Research Article

NZF Nanoscale Particles: Synthesis, Characterization and its Effective Adsorption of Bromophenol Blue

Benhadria Naceur[1], Elaziouti Abdelkader[2]*, Laouedj Nadjia[1], Sari Esmahene[1]

[1]*Laboratoire de Chimie des Matériaux Inorganiques et Application L.C.M.I.A., Université des Sciences et de la Technologie d'Oran Mohammed Boudiaf (USTO M.B.), BP 1505 El M'naouar, 31000 Oran, Algérie*

[2]*Laboratoire des Sciences Technologie et Génie des Procédés L.S.T.G.P., Université des Sciences et de la Technologie d'Oran Mohammed Boudiaf (USTO M.B.), BP 1505 El M'naouar, 31000 Oran, Algérie*

Abstract

The ferrospinels $Ni_xZn_{1-x}Fe_2O_4$ (x = 0.0 and 0.6) nanoparticles (NPs) were successfully prepared by a sol-gel method and analyzed by TGA/DTA, XRD, SEM-EDS, UV-Vis-DRS, and pH_{IEP}. The adsorption potential of NZF NPs towards the Bromophenol blue (BPB) dye was investigated. The batch adsorption efficiency parameters were studied including contact time, pH, initial dye concentrations and catalyst dosage. Results indicated that NZF crystallized in single-phase and exhibited smaller crystallite size (49 nm vs. 59.24 nm) than that of the pristine (ZF). The SEM analysis showed that the materials are elongated-like shape. NZF catalyst showed a red-shift of absorption bands and a more narrowed band gap (2.30 eV vs. 1.65 eV) as compared to ZF. The adsorption process was found to be highly dependent to the pH of the solution, dye concentration and adsorbent dose. Under optimum conditions of 5 mg.L^{-1} BPB, 0.5 g.L^{-1} NZF catalyst, pH = 6, and 25 °C, up to ≈ 86.30% removal efficiency could be achieved after 60 min. Pseudo-second-order kinetic model gave the best fit with highest correlation coefficients (R^2 ≥ 0.99). A high specific surface area, a stabilized dispersion state of NZF NPs and the electrostatic interaction between the BPB^{-2} anions and the NZF-H_3O^+ active sites on NZF surface were believed to be the main factors that can be responsible for the high adsorption efficiency. Copyright © 2020 BCREC Group. All rights reserved

Keywords: Sol-gel method; $Ni_{0.6}Zn_{0.4}Fe_2O_4$; Bromophenol blue; Characterization; Adsorption efficiency

1. Introduction

Dye polluted water commonly originates from the industrial process, such as pharmaceutical, textile, dyeing, leather, synthetic detergent, plastic, and even house hold activities. The negative impact of these colored wastewaters on the wildlife causes a tremendous environmental problem in the world in terms of ecology and sustainable development [1]. The wastewater treatment of the industrial effluents is being a primary concern of the scientific society. Conventional processes for removing colored wastewaters, including ion exchange, adsorption, chemical precipitation, membrane filtration technologies, and electrochemical treat-

* Corresponding Author.
E-mail: abdelkader.elaziouti@univ-usto.dz; elaziouti_a@yahoo.com (E. Abdelkader)
Tel.: +213-05-40288630, Fax: +213-41-500056

ment. Among these established techniques, the adsorption process has been found to be simple, efficient and economic for environmental remediation [2,3].

In this context, the use of the normal spinel Zinc ferrite or franklinite ($ZnFe_2O_4$) or modified spinel with appropriate properties can be benefit in the field of adsorption and catalysis [4]. Recently, $ZnFe_2O_4$, with a typical band gap E_g of about 1.9 eV [5], which enables it to absorb sunlight up to 653 nm or even larger, has potential application as the Fenton-like heterogeneous catalysts in the oxidation processes of refractory contaminant. However, due to their low valence band potential and poor quantum efficiency, $ZnFe_2O_4$ can not be used directly in the photocatalysis processes [6]. In the band gap engineering the solar light activated catalysts can be applied by transition metals doping for size-controlled functional nanomaterials [7-11] or for effective photoinduced electron–hole pair's separation, including semiconductor combination with matching band potentials [6,11-18]. It is worthwhile to note that these catalysts based iron-containing compounds when used directly in solution, often give rise to particle agglomeration with severe loss of effective surface area due to the magnetic interactions. However, doping with transition metal, such as Ni^{+2}, Mn^{+2}, Co^{+2}, Cu^{+2}, etc. into the spinel $ZnFe_2O_4$ nanostructures, could be able to control the particle size, efficiently avoid particles from agglomeration, and hence improve the structural, morphological, magneto-optical, and heterogeneous Fenton-like activity.

Among the nanostructured spinel ferrite materials, the iron nickel zinc based ferrites ($Ni_xZn_{1-x}Fe_2O_s$) have much interesting properties such as high saturation magnetization, high resistance and low eddy current losses [19]. This material has potential applications in the field of microelectronics, and magneto-optics, catalysts, absorbent, sensors, electronic devices and in water splitting photoelectrochemical process [20-25]. Up to now, various synthetic approach have been developed to synthesize nano-sized particles of ferrite materials, like sol–gel, hydrothermal, solvothermal, co-precipitation, microwave combustion and citrate precursor method [26-32]. Conversely, some disadvantages of the pre-cited methods like high-energy consuming, long reaction time in complicated equipment at high temperature, the use of a strong base.

Recently, much attention has been devoted to sol-gel method for the elaboration of nano-ferrite functional materials [33-35]. The method gives inorganic materials with high purity under mild conditions [36]. In this study, Ni-doped $ZnFe_2O_4$ nano-catalyst was prepared by simple sol-gel route. The material is less explored in the field of sorption of organic pollutant including dyes and other organics. The as-synthesized $Ni_{0.6}Zn_{0.4}Fe_2O_4$ (is denoted as NZF) catalysts was in detail characterized by Differential Thermal Analysis (DTA) - Thermo Gravimetric Analysis (TGA), X-ray diffraction (XRD), Scanning Electron Microscopy (SEM-EDS), pH_{IEP}, and UV-vis Diffuse Reflectance (UV-Vis-DRS) techniques. The impact of Ni-content (x) on the crystallographic, morphology and optic properties of NZF was studied. The adsorption activity of NZF catalyst were investigated in the removal of Bromophenol blue dye (BPB), as a target contaminant, from simulated wastewater. We have also explored systematically the effects of the operational conditions such as reaction time, pH of the solution, the dye concentration and catalyst dosage on the efficiency of adsorption. The removal reactions as function of time were fitted with the pseudo-second-order kinetic model. Based on the studied properties of the material, a mechanism of the increased adsorption activity of NZF catalyst was elucidated.

2. Materials and Method

2.1 Materials

All reagents, including $FeSO_4.7H_2O$, $Zn(COO)_2.6H_2O$, $NiCl_2.6H_2O$, Citric acid, and Bromophenol blue (3′,3″,5′,5″-tetra bromo phenol sulfonphthalein with the highest purity available were purchased from Sigma Aldrich. The chemical structure and physicochemical properties of Bromophenol blue dye are presented in Table 1.

2.2 Catalyst Characterizations

To determine the desired temperature for phase NZF formation, the sample was analyzed thermally by NETZSCH STA 449F3 STA449F3A-1085-M Instrument (DTA-TG 1000 °C) under a nitrogen atmosphere with a heating rate of 5 °C/min, from room temperature to 1000 °C. X-ray diffraction (Bruker D8 Advance) was performed to characterize the phase and structure of ZF and NZF nanoparticles using Cu-Kα radiation at angle ranging from 10 to 80° and a scanning rate of 10 °/min. The average crystallite size of the synthesized catalysts is calculated from the full-width-half-maximum (FWHM) of the diffraction peaks using Scherrer Equation (1) [37].

$$d_{XRD} = \frac{0.9\lambda}{\beta \cos\theta} \tag{1}$$

Where d_{XRD}, λ, β, θ are the average crystallite size, the wavelength (1.5406 Å), the full-width at half maximum (FWHM) of the intense peak in radians and Bragg angle. The size and the morphologies of the sample were examined using Jeol JSM 6360LV. Scanning Electron Microscope coupled with EDS (SEM-EDS) analysis was carried out by using Jeol JSM-6410. UV–vis spectrophotometer (Perkin Elmer Lambda 650) for UV–vis diffuse reflection spectra from 900 to 200 nm. The band gap energy (E_g) of prepared nanoparticles can be found using Kubelka-Munk (K-M) model [38]. The absorption wavelength (λ) of a solid and its' band gap value can be given by the Equation (2).

$$E_g = 1240/\lambda \tag{2}$$

The residual pollutant concentrations during adsorption process were monitored with UV Spectrophotometer (Shimadzu UV mini-1240) in the range 200 - 800 nm, using 1 cm optical pathway cells.

Polycrystalline spinel ferrite with formula $Ni_{0.6}Zn_{0.4}Fe_2O_4$ (denoted as NZF) was synthesized by the reaction of metal salts (M) including $FeSO_4.7H_2O$, $Zn(COO)_2.6H_2O$, and $NiCl_2.6H_2O$ (molar ratio $Ni^{2+} : Zn^{2+} : Fe^{3+} = x : 1-x : 2$ in distilled water with citric acid (CA) (M:CA of 1:1,1) with vigorous stirring. The obtained brown red solution was kept under stirring at room temperature for 24 h. The precipitated product was separated and thoroughly washed with distilled water and ethanol for three times and lastly dried in an oven at 80 °C for 24 h under normal pressure. At the end, samples were crushed and heated at 900 °C during 4 h. For comparison purpose, $ZnFe_2O_4$ (denoted as ZF) was also prepared in the similar route by calcination of solid Zinc ferrite particles at 1000 °C during 4 h.

2.3 Adsorption Experiment

Typically, 50 mg of adsorbent (i.e. ZF and NZF) was poured in 100 mL of BPB dye solution (10 mg/L). Before adsorption, the pH of each solution was adjusted in the range of 6-11. The adsorption was monitored at 25 °C in the dark for 60 min until equilibrium. After each 10 min, 5 mL of dye samples were centrifuged and analyzed by UV–vis spectrophotometer (Shimadzu UV mini-1240) at λ_{max} (592 nm) of BPB solution. The adsorption capacity q (mg/g) was calculated by Equation (3).

$$q = \left[\frac{(C_e - C_t)}{m}\right] v \tag{3}$$

The removal efficiency of the catalyst η (%) is expressed using Equation (4).

$$\eta = \left[\frac{(C_i - C_f)}{C_i}\right] x100 \tag{4}$$

where q is the adsorption capacity of the adsorbate (mg/g), m is the weight of adsorbent (g), vis the volume of solution (L), vis the volume of solution (L), C_e and C_t are the concentrations of the dye at equilibrium and at time t, respectively, C_i is the initial dye concentration (mg/L), and C_f is the residual dye concentration after adsorption equilibrium (mg/L).
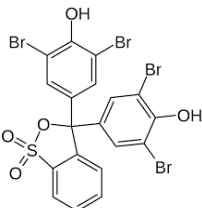
3. Results and Discussion
3.1 Characterization of the Powder

The DTA-TGA thermogram of the $Ni_{0.6}Zn_{0.4}Fe_2O_4$ (NZF) NPs is illustrated in Figure 1. The thermal decomposition of NZF proceeds with three main decomposition steps. The first weight loss occurred mainly in the range from 25 to 120 °C, corresponding to the exothermic peak in the TDA curve, namely at 120 °C.

The weight loss associated with this state (i.e. 18%) corresponding to the evaporation of adsorbed water molecules from NZF surface in

Table 1. Chemical structure and physicochemical properties of Bromophenol blue dye [57]

Bromophenol blue	Characteristics	
	Atomic composition	$C_{19}H_{10}Br_4O_5S$
	λ_{max} (nm)	592
	Molar mass (g/mol)	669,961
	pKa	3 (yellow<3)
		4.6 (blue > 4.6 and
		green 3-4.6)

perfect consistency with the reported works in the literature [39,40]. In the temperature range 120-425 °C, a second weight loss was observed, corresponding to the exothermic peaks in the TDA curve, namely at 250 °C and 425 °C, with respect to the output of the trapped water and the decomposition of the citrate network, respectively, representing weight loss of about 29%. The third weight loss (≈11%) occurred mainly from 445–750 °C and leveled off when the temperature approached 750 °C. The removal of organic impurities still remaining in the material after 800 °C. Therefore, sample was annealed from 900 °C to investigate the formation of the NZF phase.

Typical XRD patterns of spinel ZF and NZF samples are depicted in Figure 2. The diffraction peaks are the reflections corresponding to the *hkl* planes (111), (220), (311), (222), (400), (422), and (511). These diffraction peaks confirm the formation of cubic spinel structure of crystal (space group Fd-3m and JCPDS CARD 01-1108). There is no additional peak dealing with impurities. As shown in Figure 3 and Table 2, the decrease in the intensity of peaks as well as the shift in their positions to higher value of 2θ were observed in the XRD patterns of NZF as compared to ZF is an indicative of lattice cell parameter reduction for the cubic NZF sample with Ni-content (x=0.6) with low crystalline material. The average crystallite

size was estimated by Scherrer's equation using the broadening of the (311) peak. The results are shown in Table 2. The undoped ZF exhibited a crystallite size of 59.24 nm and it is reduced to 49.00 nm with Ni doping (NZF).

The peak broadening in XRD pattern is an indicative of smaller nanoparticle sizes [41]. The lattice constants "a" of the samples calculated from their corresponding XRD pattern data are obtained by Fullprof program are displayed in Table 2. The results showed a decrease in lattice parameter values from 8.4404 Å (ZF) to 8.3857 Å (NZF) with Nickel content (x=0.6). This finding is in constancy with gradual substitution of Zn^{2+} ions of larger ionic radius in ZF spinel by Ni^{2+} ions with smaller ionic radius (0.83 Å vs 0.74 Å) in NZF nanoparticles [42-46]. The lattice parameter "a" is in good agreement with the standard JCPDS value of 8.441 Å (JCPDS No. 22-1012).

The theoretical density (D_t) and specific surface area (S_S) of nano-catalysts were evaluated by Equations (5) and (6).

$$D_t = \frac{Z M_c}{a_{exp}^3 N} \qquad (5)$$

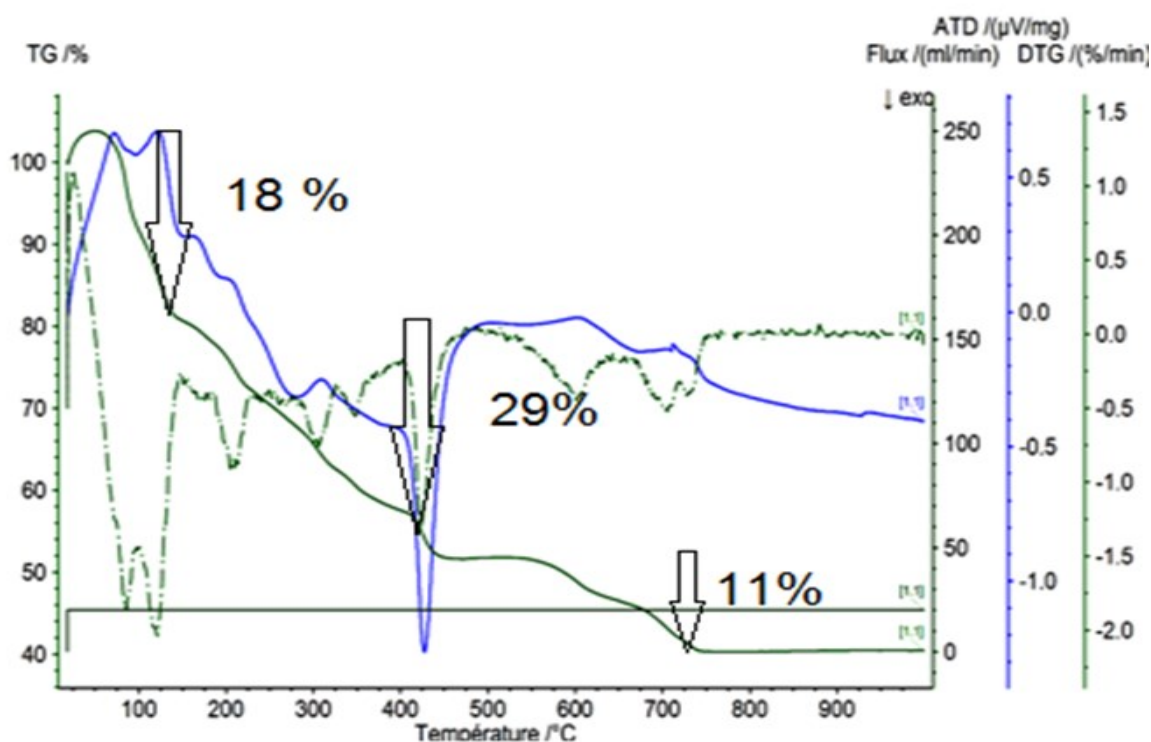$$S_s = \frac{6}{D_t d_{XRD}} \qquad (6)$$

Figure 1. TGA-DTA plots of the dried gel for NZF sample

where Z is equal to 8 chemical species in the unit cell of spinel lattice , M_c is the molar mass of the sample (g.mol^{-1}), a_{exp} is the lattice parameter of the ferrite (Å), and N is Avogadro's number (6.022×1023 mol^{-1}). The theoretical density (D_t) is given in Table 2. The results showed an increase of D_t from 5.325 to 5.338 g/cm^3 as the Ni-content (x) increases from $x=0$ to $x= 0.6$. These should give specific surface areas of ~19.02 for ZF and 22.94 m²/g for NZF.

The morphologies and structures of the magnetically ferrospinel NZF NPs were investigated using SEM images (Figure 4 a–c). Typical low-resolution SEM images, as seen in Figure 4 a-b, clearly reveal that NZF consisted of large randomly shaped aggregates of smaller individual ultrafine NPs. Particles with size up to 500 nm constituted from ultrafine particles were observed. As the particles are very small, so they get aggregated to certain extent due to high surface-to-volume ratio as well as magnetic interactions.

The NZF nanoparticles were further characterized with EDX analysis. As illustrated in Figure 5c, the relative atomic abundance of O, Fe, Ni, and Zn elements present in NZF nanocatalyst are 64.33, 24.59, 6.99, and 4.09 %, respectively. Furthermore, the atomic ratio O/Fe (2.6) is slightly higher than 2 which is an indic-

ative of intrinsic defects in the crystalline stricture (as mentioned in XRD analysis). Basically, great number of available active sites is present in samples with intrinsic oxygen vacancy defects. This can be benefit for the heterogeneous Fenton-like reactions in terms of reactivity and selectivity.

The pH drift method was used to find the isoelectric point of NZF NPs catalyst. Typically, 150 mg of NZF NPs was added to a solution of NaCl (50 mL, 0.01 M) at room temperature and pH adjusted initially (pH$_i$) from 4 to 10. The final pH (pH$_f$) was determined after 48 h. The value of IEP can be found by plotting ΔpH versus initial pH$_i$ as shown in Figure 5. The pH of zero charge of NZF NPs was found to be 6.75. This is an indication that the surface of the material is negatively charged at pH values above 6.75. While at pH under 6.75, the surface is positively charged.

The optical absorption properties of the spinel ZF and NZF nano-catalysts were investigated by UV-Vis-DRS. As depicted in Figure 6, the pristine ZF show high absorption in 200–600 nm region which is typical to ferrite based nanosystems, which may have orbital contributions from 3d^4-4s^1, 3d^5 and 4S [47,48]. ZF and NZF nano-catalysts exhibit a well-defined absorbance edges in the visible region at around

Table 2. Crystallographic parameters of the spinel ZF and NZF

Catalysts	2θ (radians)	q (Å)	FWHM (radians)	d_{XRD} (nm)	D_t g/cm^3)	S_s (m²/g)
ZF	35.2380	8.4404	0.1407	59.24	5.325	19.02
NZF	35.4754	8.3857	0.1664	49.00	5.338	22.94
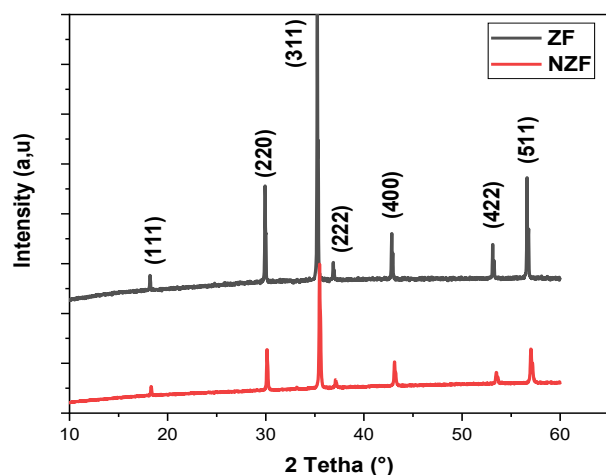
Figure 2. X-ray diffraction patterns of spinel ZF and NZF
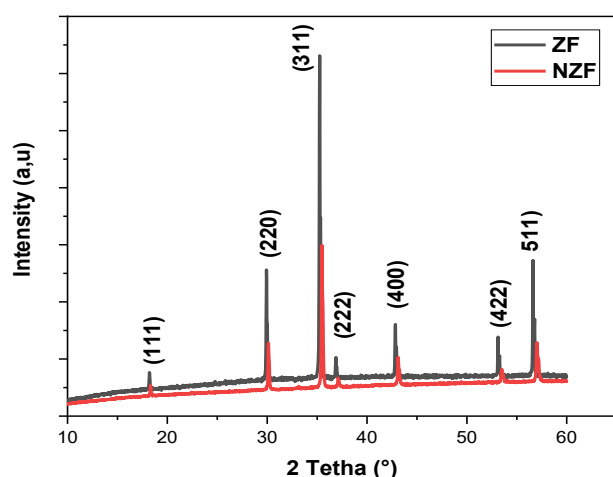
Figure 3. Superposition of X-ray diffraction patterns of spinel ZF and NZF

at 600 and 780 nm, respectively. This result gives us that both catalysts can be activated in the visible light region. The band structure is generally defined by taking the O2p orbital as the VB and the Fe3d orbital as the CB. The absorption of ferrospinels in the visible light region is due to the electron excitation from O2p into the Fe3d level. Compared with the absorbance edges of ZF, the absorption edge of NZF nano-catalyst have displaced to the higher wavelength due to the presence of high rate of crystalline defects and thus creation of novel intermediate energy levels between the VB and CB. These levels allow the promotion of electrons from VB to CB energy level. As shown in Figure 6, the two absorption edges in DRS spectrum of NZF spinel indicated the presence of two crystallite phases in NZF catalyst [49]. The optical properties of the ZF and NZF are collected in Table 3. The plot of the modified K-M function by Equation (7) permitted to find the band gap energy (E_g).

$$\alpha h v^{1/n} = \beta\left(h v - E_g\right) \tag{7}$$

with α is the linear absorption coefficient, h is the Planck's constant, v is the light frequency, E_g, and β are band gap energy and a constant involving properties of the bands respectively. The E_g values were calculated using the Tauc plotting of $(\alpha h v)^2$ vs. $h v$ and $(\alpha h v)^{1/2}$ vs. $h v$ for indirect and direct transitions, respectively, by extrapolating the straight line of these plots to $(\alpha h v)^2 = 0$ and $(\alpha h v)^{1/2} = 0$, as shown, respectively

Table 3. Optical parameters: n, λ_{max}, and E_g, for ZF and NZF

Catalysts	n	λ_{max} (nm)	E_g (eV)
ZF	2	539	2.30
NZF	1/2	751.51	1.65
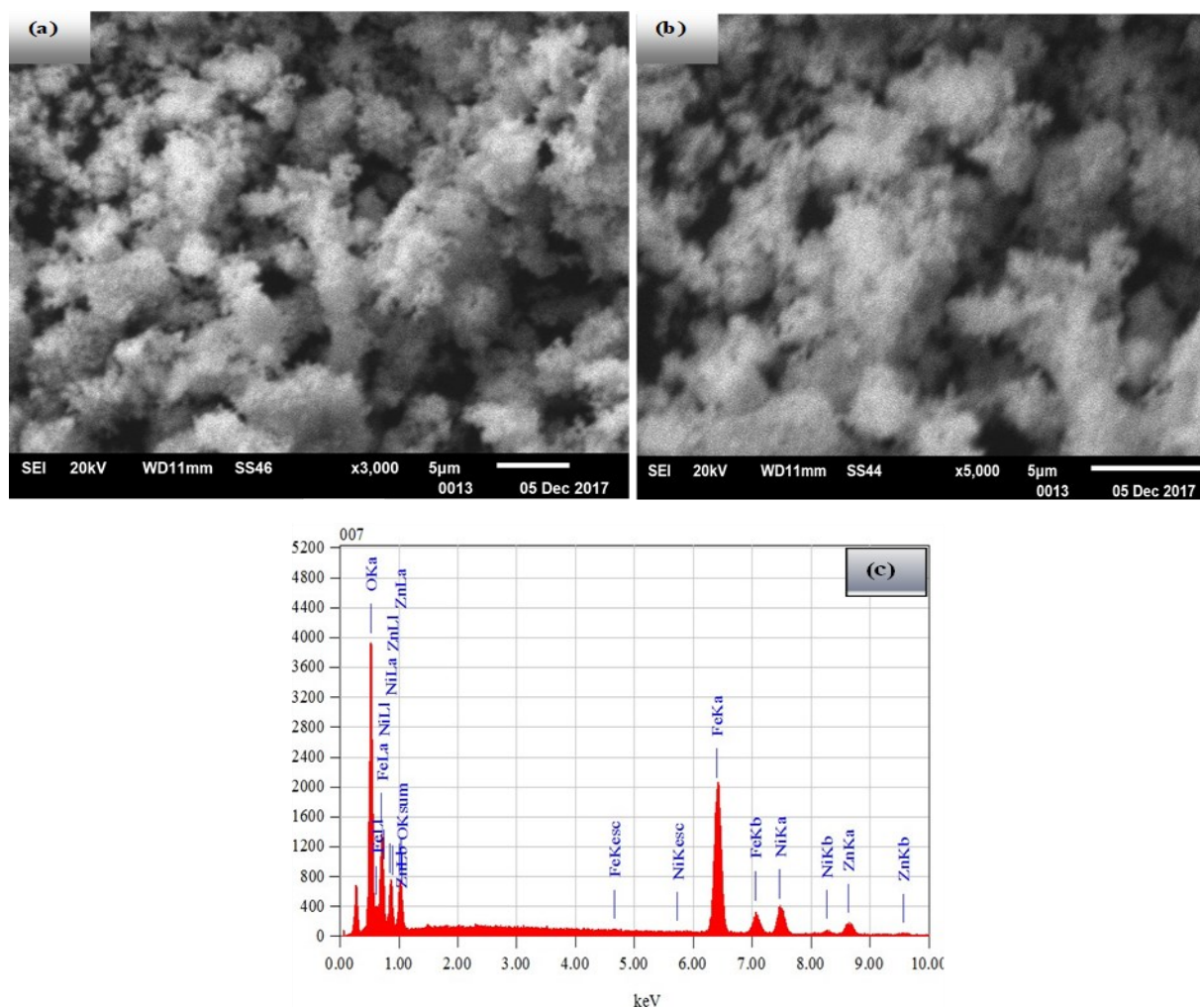
Figure 4. Micrography SEM for NZF: (a-b) Low-resolution SEM, and (c) EDX analysis for NZF

in Figures 7 and 8. The Table 3 indicates the E_g values for ZF and NZF. Based on the above reported results in Table 3 and Figures 7 and 8, for indirect transitions the E_g value for ZF was estimated to be 2.30 eV, while for NZF was 1.65 eV (direct transition).

3.2 Adsorption Kinetic

3.2.1 Effect of pH solution

Qualitative study of the evolution of absorption band maxima of BPB in aqueous solution at various pH: BPB is a redox indicator dye which shows color transition in the range from 3 to 6. The color of BPB solution is yellow at pH = 3, and exhibits bluish purple color at pH > 4.6. BPB exhibits two pKa values (pKa$_1$ = 3 and pKa$_2$ = 6) with absorption maxima at 440 nm and 592 nm in the visible region. Figure 9 depicts the dissociation equilibrium of the pH indicator BPB. Thus, BPB displays three forms: neutral form (BPB) at pH < 3 (pH < pKa$_1$), first anionic form (BPB⁻) lays between pH 3 and 4.6 (pKa$_1$ < pH <

pKa$_2$) and second anionic form (BPB^{-2}) at pH > 4.6 (pKa$_1$ < pKa$_2$ < pH).

Figure 10 illustrates the UV-visible spectra of BPB in aqueous solution at various pHs. At neutral pH (i.e. pH = 6.5 and C_0 = 10 mg/L), BPB exhibited a main band at 592 nm and associated with two absorption bands in the ultraviolet region appeared at 308 and 380 nm. As can be seen in Figure 10, under neutral and alkali media (i.e. pH ≥ 6), BPB molecules exhibited constant absorption bands with same intensities while they are most sensitive to the pH of the solution under acidic media (i.e. pH = 2 and 4).

As the value of pH of solution decreases at 4, a new band in the region 440 nm appears in the spectrum attributed to the π→π* transition in the C=C–C=O and C=C–C=C links. These absorption bands correspond to the color changes of the Bromophenol blue from blue (BPB^{-2}) to purple (BPB^{-1}). One should keep in mind that the concentration of neutral BPB form is higher than the anionic form. Further decrease in pH beyond 4 (i.e. pH = 2), the main band of BPB
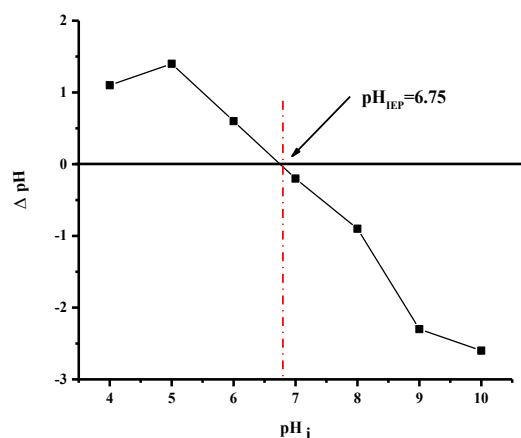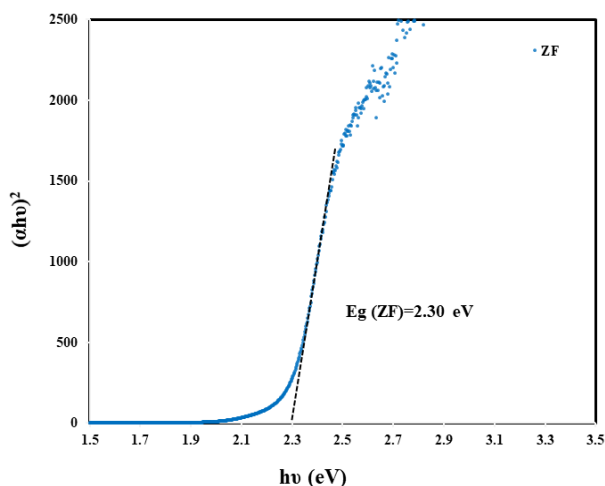

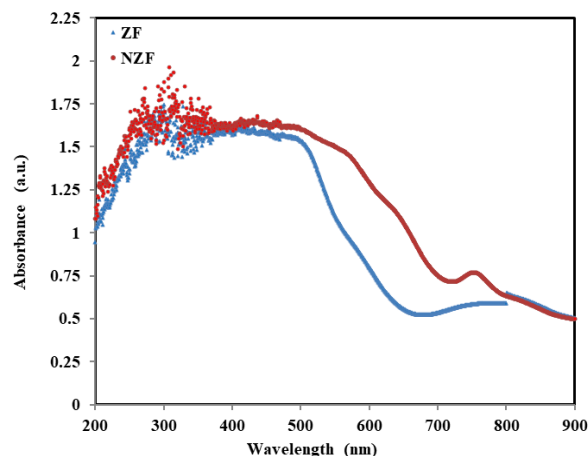**Figure 5**. The IEP of NZF nano-catalyst

Figure 6. DRS spectra of ZF and NZF

Figure 7. $(ah\upsilon)^2$ versus $h\upsilon$ plot of ZF

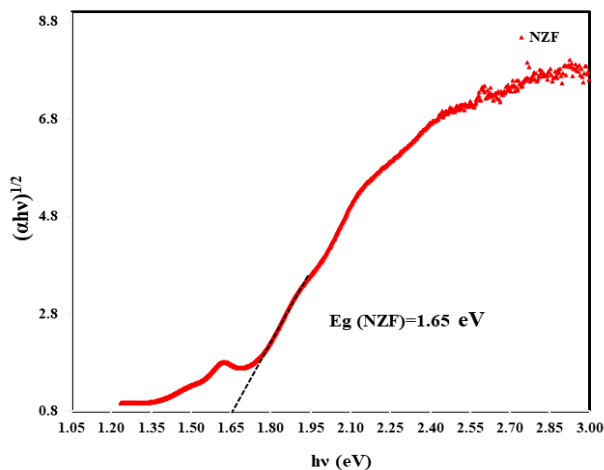**Figure 8**. $(ah\upsilon)^{1/2}$ versus $h\upsilon$ plot of NZF

blue shifted from 592 nm (anionic species BPB^{-2}) to 440 nm (neutral and yellow form BPB). A such hypochromic shift (H-bands) compared to the monomeric species are attributed to the partially self-association of BPB monomers in solution and the change in environmental conditions such as polarity of the solvent will result in solvatochromism, which is due to the strong intermolecular van der Waals-like attractive forces between the BPB molecules. The isosbestic point, at 490 nm present in the absorption spectra confirms the equilibrium between acid (BPB or BPB^{-1}) and basic (BPB^{-2}) forms in the Bromophenol blue samples [50]. For that reason, the adsorption process was conducted at pH ≥ 6.

Quantitative study: the evolution of the degradation efficiency of BPB in aqueous solution at various pH: The pH of the wastewater is one of the vital parameters that determine the efficiency of adsorption process. Thus, the experiments were conducted over a range of pH values from 6 to 11 at a fixed dye concentration (5 mg.L^{-1}), catalyst dosage (0.5 g/L of NZF) and 25 °C within 60 min of reaction. The plot of the adsorbent amount against time was illustrated in Figure 11. As shown in Table 4, the adsorption efficiency decreased from 86.30 to 4.27% as pH was increased from 6 to 11. The optimum pH of the BPB dye was 6. At this pH, the removal is maximum (up to 90.38 %) was achieved within 60 min. The link between the

**Table 4**. Pseudo-second-order kinetics parameters for adsorption of BPB at various pH solution

	Experimental results			Pseudo-second order				Pseudo-first order		
pH	η (%)	$q_{e.exp}$ (mg/g)	$q_{e.cal}$ (mg/g)	K_2 (g/mg.min)	h (mg/g min^{-1})	R^2	$q_{e.cal}$ (mg/g)	K_1 (min^{-1})	R^2
6	86.30	16.17	17.98	0.035	11.47	0.994	9.62	0.049	0.832
8	73.15	14.64	14.06	0.131	25.84	0.995	5.24	0.049	0.584
11	4.27	1.05	1.03	0.214	2.43	0.984	1.00	0.049	0.714
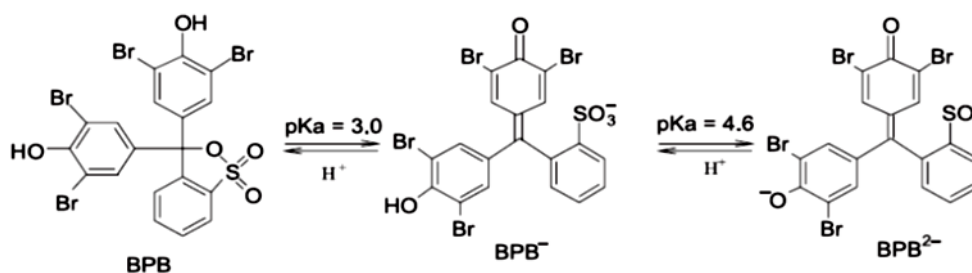
Figure 9. Dissociation equilibrium of the pH indicator Bromophenol Blue (BPB)
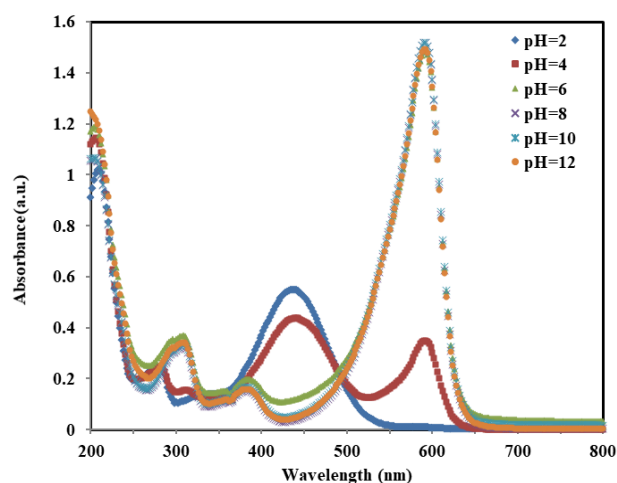

**Figure 10**. Effect of pH on the UV-visible spectra of BPB dye in aqueous solution
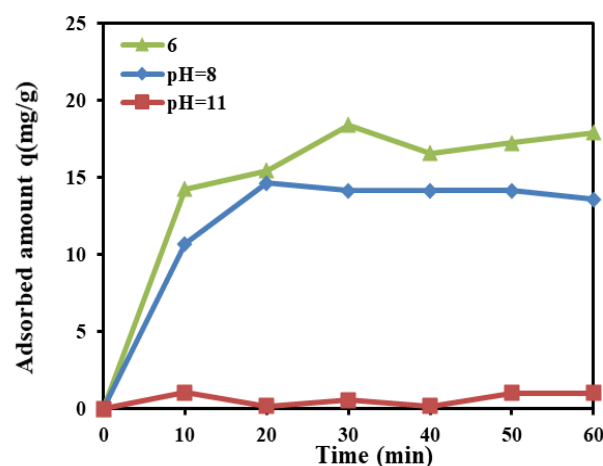
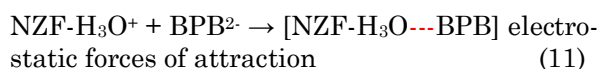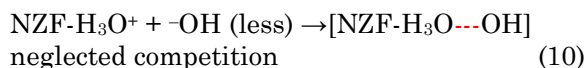**Figure 11**. Effect of pH solution on the adsorbed amount of BPB

layer charge density and the sorption-desorption reactions can be explained by the Surface Complexation Model (SCM) [51]. In the 2-pK approach, we assume that most of the semiconductor oxides are amphoteric in nature, can associate or dissociate proton in aqueous solution. The IEP (the pH of zero point charge) of NZF nano-catalyst was about 10.2 [52]. The catalyst surface has a net positive charge at $6 \leq$ pH < IEP, according to the following reaction (Equation (8)).
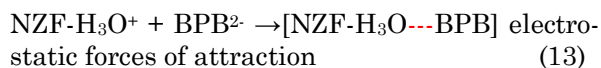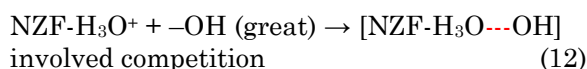
$$NZF + H_3O^+ \rightarrow \equiv NZF\text{-}H_3O^+ \quad pH < IEP \quad (8)$$
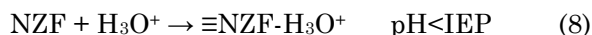
NZF surface becomes negatively charged for pH > IEP, given by the following reaction (Equation (9)).

$$NZF + OH^- \rightarrow NZFO^- + HO_2 \quad pH > IEP \quad (9)$$
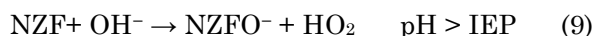
BPB is a redox indicator dye which has two functional groups (i.e. sulfonic acid group $(\text{-}S(O^3)^-)$ and oxyl group (O^-)). Under weak acidic medium (i.e. pH=6 < pKa < IEP), BPB is having strong negative charges in water (BPB^{2-}). The surface of NZF with more positively charged ($NZF\text{-}H_3O^+$) and concentration of –OH was less important to struggle with BPB^{2-} anions for vacant adsorption sites (Equation (10)), favoring adsorption of anionic form (BPB^{2-}) as a result of increased electrostatic force of attraction, as shown in Equation (11).

$$NZF\text{-}H_3O^+ + {}^-OH \text{ (less)} \rightarrow [NZF\text{-}H_3O\text{---}OH]$$
neglected competition (10)

$$NZF\text{-}H_3O^+ + BPB^{2-} \rightarrow [NZF\text{-}H_3O\text{---}BPB] \text{ electro-}$$
static forces of attraction (11)

The removal efficiency of NZF towards the BPB was high at pH = 6. However, when pH solution was increased up to 8 (pKa < pH < IEP), a slight decrease in the removal efficiency of BPB (up to 73.17%) was achieved within 60 min. At pH 8, the surface charge of NZF is less positively charged and the number of –OH was great than BPB^{2-} anions. So, there have been a competitive adsorption between anions which reduce the dye adsorption (Equations (12-13).

$$NZF\text{-}H_3O^+ + {}^-OH \text{ (great)} \rightarrow [NZF\text{-}H_3O\text{---}OH]$$
involved competition (12)

$$NZF\text{-}H_3O^+ + BPB^{2-} \rightarrow [NZF\text{-}H_3O\text{---}BPB] \text{ electro-}$$
static forces of attraction (13)

By contrast, the adsorption efficiency of BPB was scarily low and depicts minimum efficiency (up to 4.27%) at pH 11. This might be explained on the basis of amphoteric behaviors of NZF catalyst under strong alkali media. At this pH, (pKa < IEP ≈ pH), both NZF surfaces and BPB dye were negatively charged along with very high concentration of –OH. Thus, $-S(O_3)^-$ and/or (O^-)) were unable to adsorb on the $(NZFO^-)$ surface due to the electrostatic forces of repulsion (Equations (14-16)).

$$NZFO^- + BPB^{2-} \rightarrow [NZFO^- + BPB^{2-}] \text{ electrostatic forces of repulsion}$$
(14)

$$NZFO^- + OH^- \rightarrow [NZFO^- + OH^-] \text{ electrostatic forces of repulsion} \quad (15)$$

$$BPB^{2-} + OH^- \rightarrow [BPB^{2-} + OH^-] \text{ electrostatic forces of repulsion} \quad (16)$$
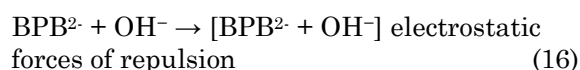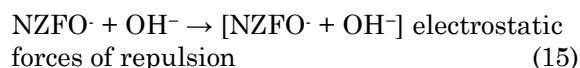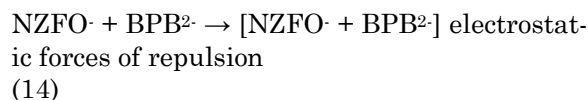
Moreover, at this pH too close to IEP and according to the principles of general colloid chemistry, an electrostatically stabilized dispersion system typically loses stability when the magnitude (i.e. absolute value) of the zeta potential decreases to less than approximately 30 mV. As a result, there will be some region surrounding the condition of zero zeta potential (i.e. the IEP) for which the system is not particularly stable. Within this unstable region, the particles may agglomerate, thereby increasing the particle size and reducing positive site of surface catalyst when transfer from neutral to basic medium. As a result, 86.30 % of dye was removed at pH = 6 within 60 min at mild conditions. Based on our results, additional research will be carried out at a pH of 6 [53].

3.2.2 Effect of time of the reaction on BPB dye removal

The effect of time on BPB removal at various equilibrium time (5–60 min) was investigated. The removal efficiency was plotted in Figure 12. A dramatically increase in the removal of BPB was observed in the initial stage (first 10 min). The removal of dye then gradually gets increased with increase of contact time up to 30 min in the second stage until equilibrium between the dye and the adsorbent. The equilibrium was reached during the optimum time of 60 min. Moreover, within 10 min the removal efficiency of 74.29 % with adsorbed amount of 14.24 mg/g of BPB were obtained. The presence of active sites on the NZF surface was believed to be responsible on the high rate of adsorption in the initial stage. However, the removal of the dye was insignificant after equilibrium. This can be explained

by the slow pore diffusion or saturation of dye molecules [54].

3.2.3 Effect of the initial BPB concentration

The effect of initial dye concentrations on adsorption process at a fixed NZF dosage (1 g/L), pH 6 and 25 °C was studied using BPB concentrations ranging between 5–40 mg/L within 60 min. As shown in Figure 13 and summarized in Table 5, the adsorption kinetic of the BPB via NZF decreased with time and then achieved equilibrium after 60 min.

The removal efficiency is slightly decreased from 86.30 to 84.74% as the BPB concentrations ranged in the field 5-10 mg/L and then scarily declined to 28.39 % as the BPB concentrations varies to 20 mg/L. At higher BPB concentrations than 20 mg/L, the removal efficiency remained almost constant. Optimum concentration of BPB dye removal (up to ≈ 86.30%) was obtained at 5 mg/L. The low initial concentration (i.e. 5 mg/L), provides the necessary Van der Waal's driving force to overcome the mass transfer resistance of BPB dye to the active surface sites of the NZF adsorbent. Moreover, the number of collisions between dye molecules was improved which increase the adsorp-

tion process. The active sites available on the surface of the NZF, are sufficient to immediately react with BPB molecules, and consequently result in an enhancement in the rate of removal of BPB (86.30 %). Further increase in dye concentration beyond 5-10 mg/L, obviously affect the adsorption yield. This will be attributed to the lesser driving force of concentration gradient between BPB and NZF catalyst, saturation of adsorption sites on the NZF surface or slow pore diffusion, and subsequently the probability of collision between BPB molecules and adsorption sites were reduced, resulting in an inadequate adsorption of BPB on the NZF surface.

3.2.4 Effect of catalyst dosage

The effect of catalyst dosage on the removal efficiency of BPB is shown in Figure 14 and the results are collected in Table 6. While keeping constant all the other operating parameters; initial BPB concentration of 5 mg/L, pH 6 and 25 °C during 60 min, the NZF dosage m/v was varied from 0.25 to 1.5 g/L. As shown in Figure
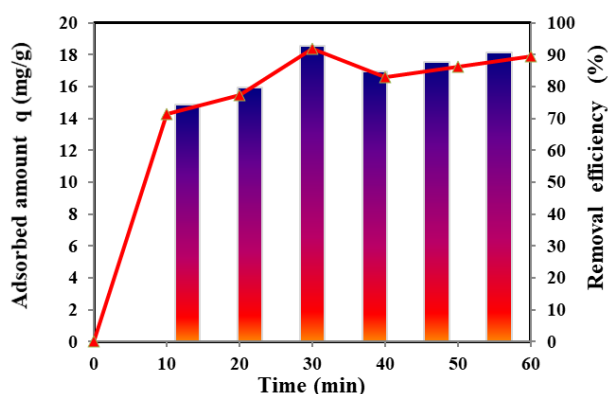

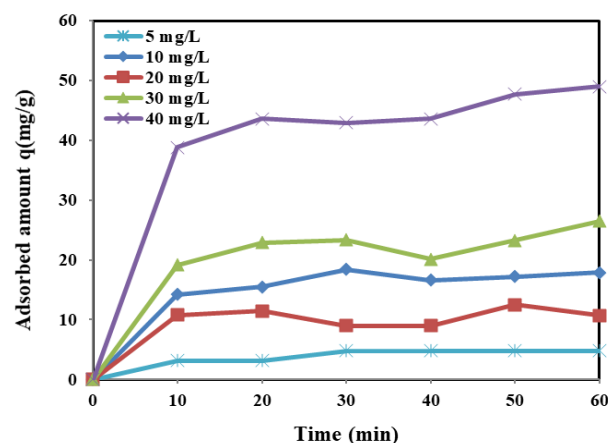**Figure 12**. Effect of time on BPB dye removal

Figure 13. Effect of initial BPB concentration on the adsorbed amount of BPB

Table 5. Pseudo-second-order kinetics parameters for adsorption of BPB at various initial BPB concentrations

	Experimental results			Pseudo-second order				Pseudo-first order		
C (mg/L)	η (%)	$q_{e.exp}$ (mg/g)	$q_{e.cal}$ (mg/g)	K_2 (g/mg.min)	h (mg/gmin^{-1})	R^2	$q_{e.cal}$ (mg/g)	K_1 (min^{-1})	R^2
5	86.30	4.76	5.13	0.042	1.10	0.9679	2.74	0.022	0.666
10	84.74	16.17	17.99	0.035	11.47	0.994	9.62	0.050	0.832
20	28.39	12.47	10.88	0.075	8.91	0.9513	4.36	0.020	0.235
30	26.26	24.48	23.92	0.485	277.77	0.9624	7.25	0.025	0.235
40	33.87	49	49.02	0.009	21.79	0.992	28.78	0.057	0.779

15, at low catalyst dosage (i.e. m/v = 0.25 g/L) a weak decrease in the removal yield (up to 21.59 %) was obtained. By increasing in the dosage of catalyst from 0.25 to 0.5 g/L, the removal efficiency was increased from 21.59 to 86.30 % and thereafter sharply decreased, almost reaching 36.07% at catalyst dosage of 1.25 g/L. Therefore, the removal of BPB was highly influenced by the amount of catalyst.

Therefore, the optimum of catalyst mass concentration was 0.5 g/L with 86.30% removal within 60 min. Scarily weak removal efficiency observed at a first catalyst dosage (i.e. 0.25 g/L) is due to the saturation of NZF catalyst surface by adsorbed matter. An increase in catalyst dosage up to 0.5 g/L would lead to more formation of the available active sites on the surface of the catalyst NZF for adsorption process, thus enhancing the removal efficiency of BPB dye. However, a decrease in the removal efficiency with further increase in catalyst dosage beyond 0.5 g/L.

According to general colloid chemistry principles, the discrepancy observed for the NZF NPs sample beyond 0.5 g/L could exclusively attributed to: (i) the electrostatically instabilized dispersion system; (ii) partially self-association of NZF NPs; (iii) low specific surface area; and (iv) less reactive sites for the adsorption of organic contaminants. The thermodynamic and mass transfer limitation and the tendency of agglomeration of NZF NPs are probably the primary factors responsible for the reduction of the removal yields. Thus, nearly complete adsorption degradation was achieved at the optimum catalyst dosage of 0.5 g/L for 60 min. Thus, 0.5 g/L of NZF was selected as the catalyst dosage for the subsequent experiments.
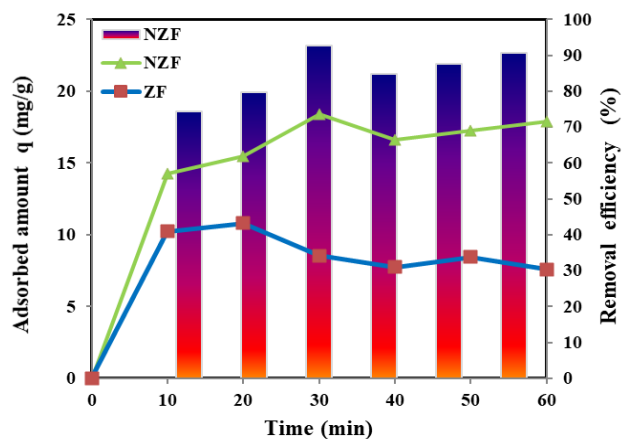
3.2.5 Effect of catalyst nature

The adsorption potential of ZF and NZF NPs toward BPB was investigated. The removal capacities of NZF compared with ZF spinel structures illustrated as NZF and ZF points in the legend of the Figure 15, are reported in Table 7. The results show also that ZF NPs depict low removal efficiency of BPB (up to 34.75%),

Table 6. Pseudo-second-order kinetics parameters for adsorption of BPB at various catalyst dosage

m/v (g/L)	Experimental results			Pseudo-second order				Pseudo-first order		
	η (%)	$q_{e.exp}$ (mg/g)	$q_{e.cal}$ (mg/g)	K_2 (g/mg.min)	h (mg/g.min^{-1})	R^2	$q_{e.cal}$ (mg/g)	K_1 (min^{-1})	R^2	
0.25 g/L	21.59	10.88	11.19	0.006	0.80	0.744	13.07	0.039	0.876	
0.5 g/L	86.30	16.17	17.98	0.035	11.47	0.994	9.62	0.049	0.832	
0.75 g/L	47.62	5.58	6.24	0.089	3.49	0.987	5.88	0.024	0.608	
1 g/L	40.43	7.05	3.07	0.059	0.55	0.927	5.94	0.073	0.963	
1.25 g/L	36.07	3.26	3.07	0.059	0.55	0.927	2.41	0.079	0.779	
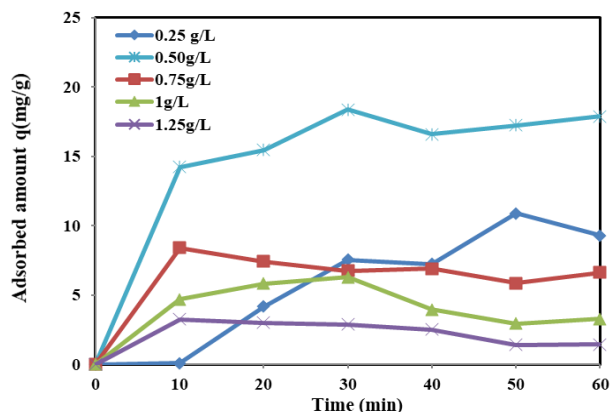
Figure 14. Effect of NZF catalyst dosage on the adsorbed amount of BPB

Figure 15. Effect of catalyst nature on the adsorbed amount of BPB (ZF and NZF points: removal capacities in mg/g, NZF bar: removal efficiency in %)

almost three times lower than that of NZF (up to 86.30 %). A great specific surface area, a stabilized and homogeneous dispersion state of NZF NPs and the electrostatic interaction between the BPB^{-2} anions and the NZF-H_3O^+ active sites on NZF surface, were believed to be the primary causes for the enhanced adsorption efficiency of NZF nano-catalyst towards BPB pollutant in comparison with that of pristine ZF. Moreover, at high temperature (T = 1000 °C in our case) leads to zinc loss during the annealing process form Ni-Zn ferrite spinels producing non-stoichiometry and resulting in cation vacancies and unsaturated oxygen ions which, due to the electrostatic interaction, bond to the neighboring Fe^{3+} ions in the spinel lattice giving rise to Fe^{2+} ions Fe^{2+}.

3.2.6 The kinetic of adsorption

Modeling with pseudo-first order: The model was developed by Lagergren as can be expressed by Equation (17) [55].

$$Log(q_e - q_t) = Log(q_e) + \frac{K_1}{2.303}t \qquad (17)$$

where q_e and q_t are the dye adsorbed per unit weight of adsorbent at equilibrium and at time t, respectively. K_1 is pseudo-first order rate constant (min^{-1}). First order rate constant k_1 was calculated from the slope value of the linear plot of log (q_e-q_t) vs. t. Correlation coefficient (R^2) was also calculated from the linear plots log (q_e-q_t) = $f(t)$. The pseudo-first-order rate constants k_2 and the correlation coefficients (R^2) at various operating keys parameters: pH of the solution, initial dye concentrations, adsorbent doses and nature of catalyst are respectively shown in Tables 4-7. The comparison between the experimental ($q_{e,exp}$) data with the calculated values ($q_{e,cal}$) does not agree well with the first-order kinetic model.

Modeling with pseudo second order: The pseudo second order kinetics equation developed by Ho and McKay, have the following linear form, Equation (18) [56]:

$$\frac{t}{q_t} = \frac{1}{K_2 q_e^2} + \frac{1}{q_e}t \qquad (18)$$

where k_2 is the pseudo-second-order constant (g/mg.min) and when time tends towards zero the initial adsorption *rate* (h (mg/g.min)) can be written as Equation (19):

$$h = K_2 q_e^2 \qquad (19)$$

where q_e is the adsorption capacity at equilibrium time, and k_2 is the pseudo-second-order constant. These two parameters can be extracted directly from the slope and intercept of plots of t/q_t vs. t, respectively at different conditions. The results are shown in Figures 16-19 and Tables 6-8. The correlation coefficient (R^2) values of the linear portions are very high, which indicates that the kinetic model of adsorption of BPB dye follows the pseudo-second-order. In this process the overall rate of adsorption was mainly controlled by chemisorption.
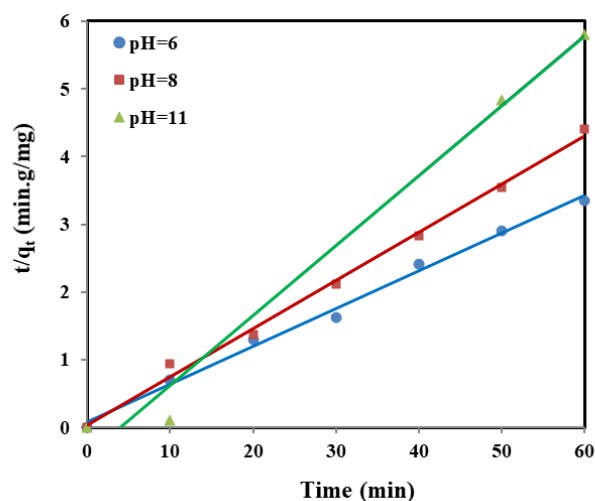
Figure 16. Pseudo-second-order kinetics for adsorption of BPB at various pH solution

Table 7. Pseudo-second-order kinetics parameters for adsorption of BPB on various catalyst

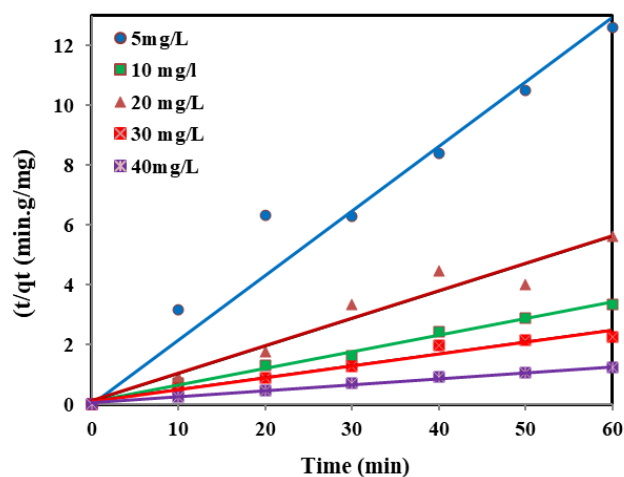| Catalysts	Experimental results		Pseudo-second order			
	η (%)	$q_{e,exp}$ (mg/g)	$q_{e,calc}$ (mg/g)	K_2 (g/mg.min)	h (mg/g min)	R^2
ZF	34.75	10.79	8.051	0.045	2.96	0.988
NZF	86.30	16.17	17.98	0.035	11.47	0.994

3.2.7 Comparison study

In comparison, the highest adsorbed amount at equilibrium was observed for Sorel's cement nanoparticles followed by NZF and ZF. This finding can be ascribed to the experimental conditions and properties of adsorbent such as specific surface area, pore size and the presence of functional groups on the external surface. The surface porosity was a factor that can be affected the uptake of the dye molecules since the BPB molecules have a large kinetic diameter in comparison with other organic molecules. Results showed that the spinel materials could be suitable for the adsorption of bromophenol blue dye. Table 8 summarizes the adsorption capacities of BPB on different adsorbents.

3.2.8 Potential adsorption mechanism

Scheme 1 shows the schematic diagram of the adsorption of BPB^{-2} anions on the $NZF-H_3O^+$ active sites of NZF clay soil, as discussed in details in the Section 3.2.1.

4. Conclusions

In this study, $ZnFe_2O_4$ (ZF) and $Ni_{0.6}Zn_{0.4}Fe_2O_4$ (NZF) stable magnetically nano-ferrospinel particles were successfully synthesized by a facile sol-gel method for removal BPB dye from the industrial aqueous media. Single phase product formation was confirmed by XRD and SEM. From XRD and UV-vis-DRS results, it is highlighted that average crystallite size and band gap energy are decreased owing to nickel ion substitution. NZF exhibited high removal efficiency (up to ~86.30%) to reduce BPB within 60 min under optimum conditions of 5 mg/L BPB, 0.5 g/L catalyst, pH = 6 and 25 °C, which was 3 times as much as that of pristine ZF. The adsorption kinetics were correlated with pseudo second order reaction. A high specific surface area, a stabilized dispersion state of NZFNPs and the electrostatic interaction between the BPB^{-2} anions and the $NZF-H_3O^+$ active sites on NZF surface, were supposed to be was the key factors
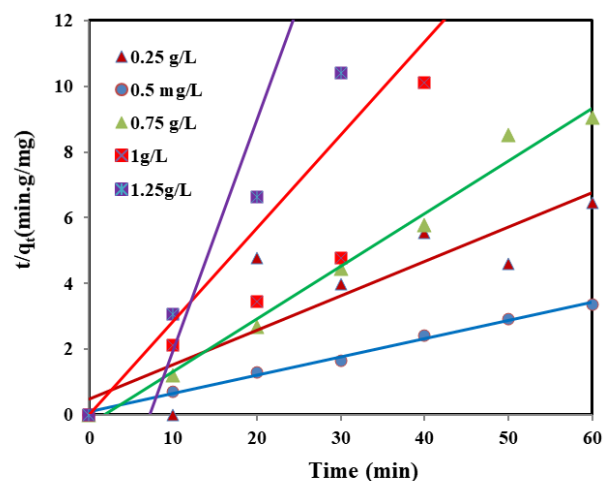

Figure 17. Pseudo-second-order kinetics for adsorption of BPB at various initial BPB concentrations

Table 8. Comparison of adsorption capacities of BPB on different adsorbents (Data after kinetic models using UV-visible apparatus)
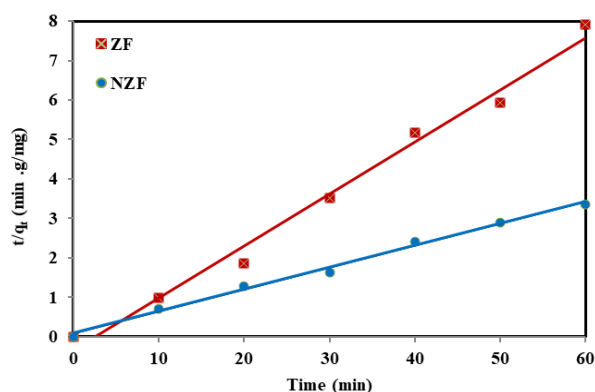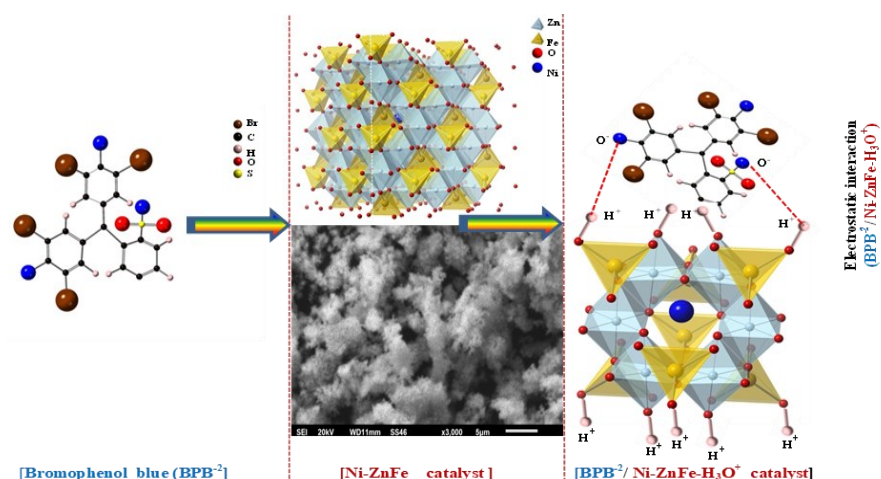
Adsorbent	C_{dye} (mg/L)	q_e (mg/g)	Refs.
α-chitin	15	22.72	[57]
Sorel's cement	7.6	28.6	[53]
CuO	45	5.82	[58]
NZF	5	16.17	This study
ZF	5	10.79	This study

Figure 18. Pseudo-second-order kinetics for adsorption of BPB at various catalyst dosage of NZF

Figure 19. Pseudo-second-order kinetics for adsorption of BPB on various catalyst

Scheme 1. The adsorption process of BPB^{-2} anions on the surface of $NZF-H_3O^+$ active sites of NZF clay soil

in the increased of the adsorption efficiency of NZF nano-adsorbent towards BPB dye. In comparison with other adsorbents, NZF was found to be a promising material for the purification of water containing BPB dye. The dye adsorption conditions, surface area, porosity and the presence of function groups on the surface could be the raisons for the high adsorption capacity of any adsorbents. The studied material could be also effective in the area of catalysis due to its appropriate band gap which can be effectively used as photocatalyst. This study gives an introduction of our future research works on these kinds of materials in the field of advanced catalysis.

Acknowledgements

References

[1] Tadjarodi, A., Imani, M., Salehi, M. (2015). $ZnFe_2O_4$ nanoparticles and a clay encapsulated $ZnFe_2O_4$ nanocomposite: synthesis strategy, structural characteristics and the adsorption of dye pollutants in water, *RSC Advances*, 5, 56145–56156. doi: 10.1039/C5RA02163D

[2] Dhananasekaran, S., Palanivel, R., Pappu, S. (2016). Adsorption of Methylene Blue, Bromophenol Blue, and Coomassie Brilliant Blue by α-chitin Nanoparticles, *Journal of Advanced Research*, 7, 113–124, doi: 10.1016/j.jare.2015.03.003

[3] Elaziouti, A., Laouedj, N., Vannier, R.N. (2016). Adsorption of Congo red on nanosized SnO_2 derived from sol-gel method. *International Journal of Industrial Chemistry*, 7, 53–70, doi: 10.1007/s40090-015-0061-9

[4] Chinnasamy, C.N., Narayanasamy, A., Ponpandian, N., Chattopadhyay, K., Guerault, H., Greneche, J.M. (2000).Magnetic properties of nanostructured ferrimagnetic zinc ferrite, *Journal of Physics: Condensed Matter*, 12, 7795-7805, doi: 10.1088/0953-8984/12/35/314

[5] Matsumoto, Y. (1996). Energy Positions of Oxide Semiconductors and Photocatalysis with Iron Complex Oxides. *Journal of Solid State Chemistry,* 126, 227–234, doi: 10.1006/jssc.1996.0333

[6] Valenzuela, M.A., Bosch, P., Jiménez-Becerrill, J., Quiroz, O., Páez, A.I. (2002). Preparation, characterization and photocatalytic activity of ZnO, Fe_2O_3 and $ZnFe_2O_4$, *Journal of Photochemistry and Photobiology: A*, 148, 177–182, doi: 10.1016/S1010-6030(02)00040-0

[7] Boudjemaa, A., Popescu, I., Juzsakovac, T., Kebir, M., Helaili, N., Bachari, K., Marcu, I.C. (2016) M-substituted (M = Co, Ni and Cu) zinc ferrite photo-catalysts for hydrogen production by water photo-reduction, *International Journal of Hydrogen Energy*, 41, 11108-11118, doi: 10.1016/j.ijhydene.2016.04.088

[8] Padmapriya, G., Manikandan, A., Krishnasamy, V., Jaganathan, S.K., Antony, S.A. (2016). Spinel $Ni_xZn_{1-x}Fe_2O_4$ $(0.0 \leq x \leq 1.0)$ nano-photocatalysts: Synthesis, characterization and photocatalytic degradation of methylene blue dye, *Journal of Molecular Structure*, 1119, 39-47, doi: 10.1016/j.molstruc.2016.04.049

[9] Gul, M., Akhtar, K. (2017). Synthesis of magnetic $ZnFe_{1.5}Al_{0.5}O_4$ nanoparticles and their photocatalytic activity testing under sunlight irradiation, *Journal of Scientific and Innovative Research*, 6, 19-24.

[10] Harish, K., BhojyaNaik, H. (2013). Solar light active $ZnFe_{2-x}Al_xO_4$ materials for optical and photocatalytic activity: an efficient photocatalyst, *International Journal of Scientific Research*, 4,301-307

[11] Cao, X., Gu, L., Lan, X., Zhao, C., Yao, D., Sheng, W. (2007). Spinel $ZnFe_2O_4$ nanoplates embedded with Ag clusters: Preparation, characterization, and photocatalytic application, *Materials Chemistry and Physics*, 106, 175-180, doi: 10.1016/j.matchemphys.2007.05.033

[12] Xie, J.S., Wu, Q.S., Zhao, D.F. (2012). Electrospinning synthesis of $ZnFe_2O_4/Fe_3O_4/Ag$ nanoparticle loaded mesoporous carbon fibers with magnetic and photocatalytic properties, *Carbon*, 50, 800-807, doi: 10.1016/j.carbon.2011.09.036

[13] Cheng, P., Li, W., Zhou, T.L., Jin, Y.P., Gu, M.Y. (2004). Physical and photocatalytic properties of zinc ferrite doped titania under visible light irradiation, *Journal of Photochemistry and Photobiology: A*, 168, 97–101, doi: 10.1016/j.jphotochem.2004.05.018

[14] Cheng, P., Deng, C.S., Gu, M.Y., Shangguan, W.F. (2007). Visible-light responsive zinc ferrite doped titania photocatalyst for methyl orange degradation, *Journal of Materials Science*, 42, 9239–9244. doi: 10.1007/s10853-007-1902-5

[15] Jin, Y.X., Li, G.H., Zhang, L.D. (2005). Electron-lattice coupling in $ZnFe_2O_4/TiO_2$ nanocomposite films, *Applied Physics Letters*, 86, 091906. doi:10.1063/1.1866503

[16] Chen, C.H., Liang, Y.H., Zhang, W.D. (2010). $ZnFe_2O_4/MWCNTs$ composite with enhanced photocatalytic activity under visible-light irradiation, *Journal of Alloys and Compounds*, 501, 168–172. doi: 10.1016/j.jallcom.2010.04.072

[17] Kaneva, N.V., Dushkin, C.D. (2011).Tuning of the UV photocatalytic activity of ZnO using zinc ferrite(III): Powders and thin films prepared of powders, *Colloids and Surfaces A: Physicochemical and Engineering Aspects*, 382, 211–218. doi: 10.1016/j.colsurfa.2010.11.031

[18] Zhang, L., He, Y., Ye, P., Wua, Y., Wua, T. (2013). Visible light photocatalytic activities of $ZnFe_2O_4$ loaded by Ag_3VO_4 heterojunction composites, *Journal of Alloys and Compounds*, 549, 105–113. doi: 10.1016/j.jallcom.2012.09.063

[19] Rashad, M.M., Fouad, O.A. (2005). Synthesis and characterization of nano-sized nickel ferrites from fly ash for catalytic oxidation of CO, *Material Chemistry and Physics.* 94, 365 – 370. doi: 10.1016/j.matchemphys.2005.05.028

[20] Satyanarayana, L., Reddy, K.M., Manorama, S.V. (2003). Nanosized spinel $NiFe_2O_4$: A novel material for the detection of liquefied petroleum gas in air, *Materials Chemistry and Physics*, 82, 21–26. doi: https://doi.org/10.1016/S0254-0584(03)00170-6

[21] Gubin, S.P., Koksharov, Y.A., Khomutov, G.B., Yurkov, G.Y. (2005). Magnetic nanoparticles: preparation, structure and properties, *Russian Chemical Reviews*, 74, 489–520. doi: DOI:10.1070/RC2005v074n06ABEH000897

[22] Frei, E.H., Gunders, E., Pajewsky, M., Alkan, W.J., Eshchar, J. (1968). Ferrites as Contrast Material for Medical X-Ray Diagnosis, *Journal of Applied Physics*, 39, 999–1001. doi: 10.1063/1.1656366

[23] Majeed, M.I., Lu, Q., Yan, W., Li Z., Hussain, I., Tahir, M.N., Tremel, W., Tan, B. (2013). Highly water soluble magnetic iron oxide (Fe_3O_4) nanoparticles for drug delivery: enhanced in vitro therapeutic efficacy of doxorubicin and MION conjugates, *Journal of Materials Chemistry B*, 1, 2874–2884. doi: 10.1039/c3tb20322

[24] Gar´cia-Jimeno, S., Ortega-Palacios, R., Cepeda-Rubio, M.F.J., Vera,A., Leija, L., Estelrich, J. (2012). Improved thermal ablation efficacy using magnetic nanoparticles: a study in tumors phantoms, *Progress in Electrom Research*, 128, 229–248. doi: 10.2528/PIER12020108

[25] Landi, G.T. (2013). Simple models for the heating curve in magnetic hyperthermia experiments, *Journal of Magnetism and Magnetic Materials*, 326, 14–21. doi: 10.1016/j.jmmm.2012.08.034

[26] Manikandan, A., Arul Antony, S., Sridhar, R., Ramakrishna, S., Bououdina, M. (2014). Simple combustion synthesis and optical studies of magnetic $Zn_{1-x}Ni_xFe_2O_4$ nanostructures for photoelectrochemical applications, *Journal of Nanoscience and Nanotechnology*, 14, 1–13. doi: 10.1166/jnn.2015.9814

[27] Manikandan, A., Durka,M., Arul Antony, S. (2014). A Novel Synthesis, Structural, Morphological, and Opto-magnetic Characterizations of Magnetically Separable Spinel $Co_xMn_{1-x}Fe_2O_4$ ($0 \leq x \leq 1$) Nano-catalysts, *Journal of Superconductivity and Novel Magnetism*, 27, 2841-2857. doi: 10.1007/s10948-014-2771-1

[28] Wang, H.W., Kung, S.C. (2004). Crystallization of nanosized Ni–Zn ferrite powders prepared by hydrothermal method, *Journal of Magnetism and Magnetic. Materials*, 270, 230-236. doi: 10.1016/j.jmmm.2003.09.019

[29] Zahi, S., Hashim, M., Daud, A.R. (2007). Synthesis, magnetic properties and microstructure of Ni–Zn ferrite by sol–gel technique, *Journal of Magnetism and. Magnetic. Materials*, 308, 177-182. doi: 10.1016/j.jmmm.2006.05.033

[30] Verma, A., Thakur, O.P., Prakash, C., Goel, T.C., Mendiratta, R.G. (2005). Temperature dependence of electrical properties of nickel–zinc ferrites processed by the citrate precursor technique, *Materials Science and Engineering. B*, 116, 1-6. doi: 10.1016/j.mseb.2004.08.011

[31] Choi, Y., Shim, H.S., Lee, J.S. (2001). Study on magnetic properties and structural analysis of Ni–Zn ferrite prepared through self-propagating high-temperature synthesis reaction by neutron diffractometry, *Journal of Alloys and Compounds*, 326, 6-60. doi: 10.1016/S0925-8388(01)01231-2

[32] Mary Jacintha, A., Manikandan, A., Chinnaraj, K., Arul Antony, S., Neeraja, P. (2015). Comparative studies of spinel $MnFe_2O_4$ nanostructures: structural, morphological, optical, magnetic and catalytic properties, *Journal of Nanoscience and Nanotechnology*, 15, 9732-9740. doi: 10.1166/jnn.2015.10343

[33] Santos, O.D., Weiler, M.L., Junior, D.Q., Medina, A.N. (2001). CO gas-sensing characteristics of SnO_2 ceramics obtained by chemical precipitation and freeze-drying. *Sensors and Actuators. B*. 75, 83-87. doi: 10.1016/S0925-4005(01)00537-8

[34] Ibarguen, C.A., Mosquera, A., Parra, R., Castro, M.S., Rodriguez-Paez, J.E. (2007). Synthesis of SnO_2 nanoparticles through the controlled precipitation routes, *Materials Chemistry and Physics*, 101, 433-434. doi: 10.1016/j.matchemphys.2006.08.003

[35] Boreddy, R. (2011). Materials and Production Engineering, University "Federico II" of Naples, Italy

[36] Elaziouti, A., Laouedj, N., Benhadria, N., Bettahar, N. (2016). SnO_2 foam grain-shaped nanoparticles: Synthesis, characterization and UVA light induced photocatalysis, *Journal of Alloys and Compounds*, 679, 408-419. doi: 10.1016/j.jallcom.2016.04.016

[37] Azàroff, L.V. (1968). Elements of X-Ray Crystallography. McGraw-Hill, New-York

[38] Chen, J.L., Chen, D., He, J.J., Zhang, S.Y., Chen, Z.H. (2009).The microstructure, optical, and electrical properties of sol–gel-derived Sc-doped and Al–Sc co-doped ZnO thin films, *Applied Surface Science*, 255, 9413–9419. doi: 10.1016/j.apsusc.2009.07.044

[39] Dey, S., and Ghose, J. (2003). Synthesis, characerization and magnetic studies on nanocrystalline $Co_{0.2}Zn_{0.8}Fe_2O_4$, *Materials Research Bulletin*, 38 (11-12), 1653-1660. doi: 10.1016/S0025-5408(03)00175-2

[40] Kandasamy, V., Vellaiyappan, S.K.V., Sechassalom, S. (2010). Synthesis of Nickel Zinc Iron Nanoparticles by Coprecipitation Technique, *Materials Research*, 13(3), 299-303. doi: 10.1590/S1516-14392010000300005

[41] Hu, C., Zhang, Z., Liu, H., Gao, P., Lin Wang, Z. (2006). Direct synthesis and structure characterization of ultrafine CeO_2 nanoparticles, *Nanotechnology*, 17,5983. doi: 10.1088/0957-4484/17/24/013

[42] Safari, A., Gheisari, Kh., Farbod, M. (2017). Characterization of Ni ferrites powders prepared by plasma arc discharge process, *Journal of Magnetism and Magnetic Materials*, 421,44-51. doi: 10.1016/j.jmmm.2016.07.024

[43] Nalbandian, L., Delimitis, A., Zaspalis, V.T., Deliyanni, E.A., Bakoyannakis, D.N., Peleka, E.N. (2008). Hydrothermally prepared nanocrystalline Mn–Zn ferrites: Synthesis and characterization, *Microporous and Mesoporous Materials*, 114, 465-473. doi: 10.1016/j.micromeso.2008.01.034

[44] Rath, C., Anand, S., Das, R.P., Sahu, K.K., Kulkarni, S.D., Date, S.K., Mishra, N.C. (2002). Dependence on cation distribution of particle size, lattice parameter, and magnetic properties in nanosize Mn–Zn ferrite, *Journal of Applied Physics*, 91, 2211-2215. doi: 10.1063/1.1432474

[45] Mohamed Ali, A., Kasim El-Sayed, R., El-Shokrofy, K.M., Abo Arais, A., Shams, M. S. (2014). The influence of Zn^{2+} ions substitution on the microstructure and transport properties of Mn-Zn nanoferrite, *Materials Sciences and Applications*, 5, 932-942.

[46] Safari, A., Gheisari, Kh., Farbod, M. (2017) . Characterization of Ni ferrites powders prepared by plasma arc discharge process, *Journal of Magnetism and Magnetic Materials*. 421, 44–51. doi: 10.1016/j.jmmm.2016.07.024

[47] Hemeda, O.M. (2004). IR spectral studies of $Co_{0.6}Zn_{0.4}Mn_xFe_{2-x}O_4$ ferrites, *Journal of Magnetism and Magnetic Materials*, 281, 36-41. doi: 10.1016/j.jmmm.2004.01.100

[48] Padmapriya, G., Manikandan, A., Krishnasamy, V., Kumar Jaganathan, S., Arul Antony, S. (2016). Spinel $Ni_xZn_{1-x}Fe_2O_4$ $(0.0 \leq x \leq 1.0)$ nano-photocatalysts: Synthesis, characterization and photocatalytic degrada-

tion of methylene blue dye, *Journal of Molecular Structure*, 1119, 39-47. doi: 10.1016/j.molstruc.2016.04.049

[49] Gao, D.Q., Shi, Z.H., Xu, Y., Zhang, J., Yang, G.J., Zhang, J.L., Wang, X.H., Xue, D.S. (2010). Synthesis, magnetic anisotropy and optical properties of preferred oriented zinc ferrite nanowire arrays, *Nanoscale Research Letters*, 5, 1289–1294. doi: 10.1007/s11671-010-9640-z

[50] Singh, J.P., Srivastava, R.C., Agrawal, H.M. (2010). Optical behaviour of zinc ferrite nanoparticles, *AIP Conference Proceedings*, 1276, 137–143. doi: 10.1063/1.3504278

[51] Nazarkovsky, M.A., Gun'ko, V.M., Wójcik, G., Czech, B., Sobieszek, A., Skubiszewska-Zieba, J., Janusz, W., Skwarek, E. (2014). Bandgap change and photocatalytic activity of silica/titania composite associated with incorporation of CuO and NiO, *Physic and Technology of Surface*, 5, 421–437. doi 10.15407/hftp05.04.421

[52] Henari, F.Z., Culligan, K.G. (2010) .The influence of pH on nonlinear refractive index of Bromophenol Blue, *Physics International*, 1, 27-30. doi: 10.3844/pisp.2010.27.30

[53] El-Gamal, S.M.A., Amin, M.S., Ahmed, M.A. (2015). Removal of methyl orange and bromophenol blue dyes from aqueous solution using Sorel's cement nanoparticles. *Journal of Environmental Chemistry and Engineering*, 3, 1702–1712. doi: 10.1016/j.jece.2015.06.022

[54] Fernandez, J., Kiwi, J., Lizama, C., Freer, J., Baeza, J., Mansilla, H.D. (2002). Factorial experimental design of Orange II photocatalytic discolouration, *Journal of Photochemistry and Photobiology. A: Chemistry*, 151, 213–219. doi: 10.1016/S1010-6030(02)00153-3

[55] Lagergren, S., Vetenskapsakad, K. S. (1898). "ZurTheorie der Sogenannten dsorption GelösterStoffe, Kungliga Svenska Vetenskapsakademiens," 24, 1–39, Handlingar,

[56] Ho, Y.S., Mc Kay, G. (1999). Pseudo-second order model for sorption processes, *Process Biochem*, 34 ,451–465. doi: 10.1016/S0032-9592(98)00112-5

[57] Solairaj, D., Rameshthangam, P., Srinivasan, P. (2016). Adsorption of methylene blue, bromophenol blue and coomassie brilliant blue by α-chitin nanoparticles, *Journal of Advanced Research*, 7, 113-124. doi: 10.1016/j.jare.2015.03.003

[58] Rashad, M., Hattem, A.A. (2019). Promising adsorption studies of bromopheol blue using copper oxide nanoparticles, *Desalination and Water Treatment*, 139, 360-368, doi: 10.5004/dwt.2019.23296